Article

Electronically integrated, mass-manufactured, microscopic robots

https://doi.org/10.1038/s41586-020-2626-9

Received: 23 October 2019

Accepted: 1 July 2020

Published online: 26 August 2020

Check for updates

Marc Z. Miskin[1,2,3]✉, Alejandro J. Cortese[2], Kyle Dorsey[4], Edward P. Esposito[2], Michael F. Reynolds[2], Qingkun Liu[2], Michael Cao[4], David A. Muller[1,4], Paul L. McEuen[1,2]✉ & Itai Cohen[1,2]✉

Fifty years of Moore's law scaling in microelectronics have brought remarkable opportunities for the rapidly evolving field of microscopic robotics[1–5]. Electronic, magnetic and optical systems now offer an unprecedented combination of complexity, small size and low cost[6,7], and could be readily appropriated for robots that are smaller than the resolution limit of human vision (less than a hundred micrometres)[8–11]. However, a major roadblock exists: there is no micrometre-scale actuator system that seamlessly integrates with semiconductor processing and responds to standard electronic control signals. Here we overcome this barrier by developing a new class of voltage-controllable electrochemical actuators that operate at low voltages (200 microvolts), low power (10 nanowatts) and are completely compatible with silicon processing. To demonstrate their potential, we develop lithographic fabrication-and-release protocols to prototype sub-hundred-micrometre walking robots. Every step in this process is performed in parallel, allowing us to produce over one million robots per four-inch wafer. These results are an important advance towards mass-manufactured, silicon-based, functional robots that are too small to be resolved by the naked eye.

Figure 1a shows a microscopic robot still attached to its substrate and Fig. 1b shows a side view of a robot after release. Each robot consists of two main parts: a body containing standard silicon electronics, and legs consisting of our newly developed actuators and panels that set the legs' three-dimensional shape. The electronics in this case are simple circuits made from silicon photovoltaics and metal interconnects. These microscopic robots walk when illuminated by a sequence of laser pulses, shown schematically in Fig. 1c and in a real micrograph sequence in Fig. 1d. Each robot is comparable in size to larger microorganisms: a robot next to a single-celled *Paramecium* is shown in Fig. 1e. All of the components are fabricated in parallel as part of the same integrated process. A chip, cut from a wafer, with thousands of microscopic robots on its surface is shown in Fig. 1f.

The key innovation enabling these microscopic robots is a new class of actuators that we call surface electrochemical actuators or SEAs (Fig. 2). SEAs are made from nanometre-thick platinum and are fabricated using standard semiconductor technologies. We grow 7-nm-thick layers of platinum (Fig. 2b, Extended Data Figs. 1, 2) using atomic layer deposition (ALD), cap the exposed surface with an inactive material, either graphene or sputtered titanium, and pattern them using lithography (Methods). Once released, the SEAs bend, due to both pre-stresses in the device (Extended Data Fig. 3) and the difference in surface stress between the platinum and the capping layer. We use the latter for actuation: when biased relative to the surrounding aqueous electrolyte, ions adsorb/desorb from the platinum surface, changing the surface stress (Fig. 2c). Videos of individual actuators (Supplementary Video 1) and parallel arrays (Supplementary Video 2) are included in the Supplementary Information.

We find three regimes of actuation: one associated with hydrogen adsorption, one associated with the adsorption of oxygen species (for example, OH^-, H_2O, $H_2PO_4^-$ and O_2^-)[12] and one associated with surface oxidation (Extended Data Figs. 4, 5). Both adsorption and oxidation lead to swelling of the platinum surface, consistent with the behaviour seen in macroscale, platinum electrochemical actuators[12–15].

Here we focus on actuation in the oxygen-species adsorption regime as the curvature change is larger than that for hydrogen adsorption, it can be accessed with lower applied voltages and the behaviour is highly reproducible. In this regime, actuators reversibly bend from flat to curled over a span of roughly 200 mV (Fig. 2d). They consume less than 10 nW of power, set by background Faradaic currents between the actuator and the electrolyte (Extended Data Fig. 5, Methods). Typical curvatures, R_c^{-1}, are on the order of micrometres (Fig. 2d) and are well described by a single-species adsorption process (see Methods for derivation)[16–18]:

$$R_c^{-1} = \frac{\gamma_m t}{2D} \frac{1}{1+\exp\left[\frac{-e}{k_B T n}(V - V_0)\right]}, \quad (1)$$

[1]Kavli Institute at Cornell for Nanoscale Science, Cornell University, Ithaca, NY, USA. [2]Laboratory of Atomic and Solid-State Physics, Cornell University, Ithaca, NY, USA. [3]Department of Electrical and Systems Engineering, University of Pennsylvania, Philadelphia, PA, USA. [4]School of Applied and Engineering Physics, Cornell University, Ithaca, NY, USA. ✉e-mail: mmiskin@seas.upenn.edu; plm23@cornell.edu; ic64@cornell.edu

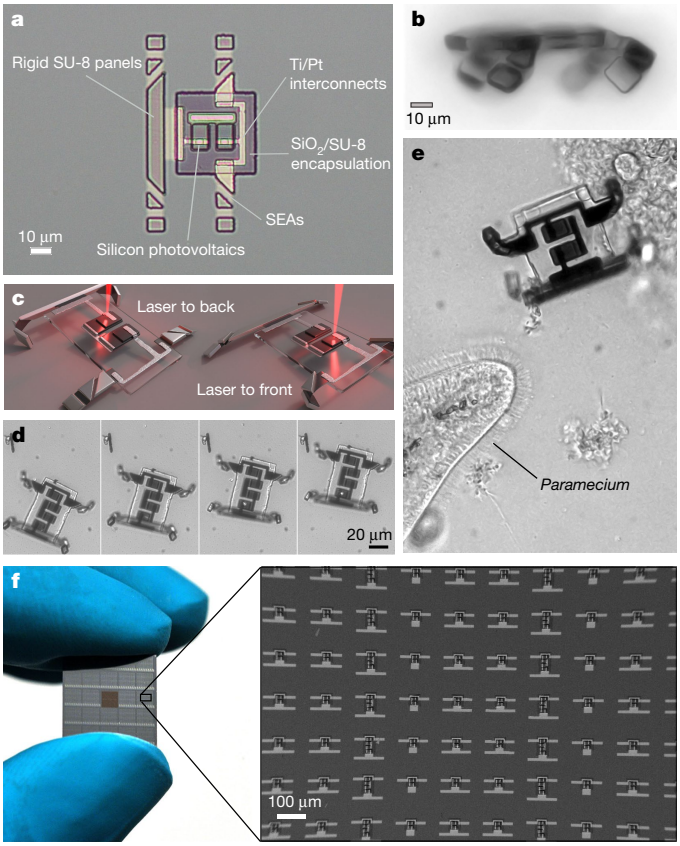

Fig. 1 | Electronically integrated microscopic robots fabricated in parallel. **a**, Optical image of a microscopic robot. It has two parts: a body with internal electronics and legs that actuate. For the work here, the electronics are simple circuits made from silicon p–n junctions and metal interconnects, encapsulated between a layer of silicon dioxide and a layer of SU-8 photoresist. The legs are made from a new class of voltage-controlled actuators called SEAs and rigid SU-8 panels. The panels control the folded shape of the leg while the SEAs produce motion. **b**, Optical side view image showing the three-dimensional structure of the folded robot. **c**, By directing laser light to photovoltaics that alternately bias the front and back legs, the robot walks along patterned surfaces. **d**, Montage of a real robot walking across a surface. Each frame is about 8 s apart. **e**, These robots are comparable to biological microorganisms; we show a micrograph of a robot beside a *Paramecium* for scale. **f**, Optical image of a chip with thousands of robots on it. The chip was cut from a four-inch wafer with approximately one million microscopic robots on its surface.

where V is the applied voltage, t is the SEA thickness, D is the bending energy, γ_m is change in surface stress from the maximum density of adsorbate on the platinum, n is a phenomenological non-ideality factor, V_0 is an offset voltage set by the free energy of adsorption, electrode composition and solution chemistry, k_B is the Boltzmann constant, T is temperature and e is the electronic charge. For the data shown in Fig. 2d, we find n is approximately 1.2, close to ideal adsorption behaviour (Methods). We further find that $D = 5 \times 10^{-15}$ J and $\gamma_m = 0.3$ N m^{-1}, consistent in scale with previous work[12,14] and material properties for bulk platinum (Methods).

In this regime, SEAs can cycle repeatably without measurable degradation (Fig. 2e) and respond in about 10–100 ms (Fig. 2f), limited by the viscous drag of the fluid and the stiffness of the cantilever[19,20]. The maximum force output is on the order of nanonewtons (Methods), about ten times larger than typical optical trap forces, comparable to those involved in cell movement[21], and more than enough to lift and move the 50 pN weight of the robot's body (adjusted for buoyancy). Broadly, SEAs can be used in any application where a micrometre-scale actuation is needed. Furthermore, any electrical power source capable of supplying voltages of 200 mV and about 10 nW of power can function as a controller, most notably, standard silicon microelectronics.

These results show that SEAs meet all the requirements for electronically controlled, microscale robot actuators: small radii of curvature, low-voltage actuation, low power, substantial force output

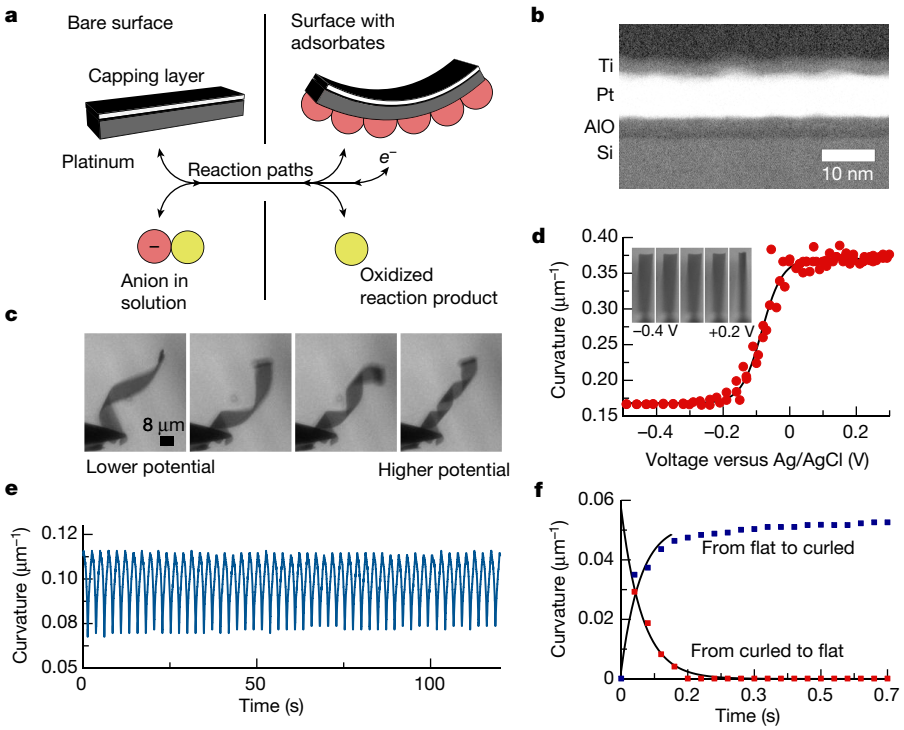

Fig. 2 | Platinum-based SEAs. **a**, Schematic of a SEA bending in response to electrochemically driven adsorption. This reversible process is controlled by the potential between the actuator and the electrolyte. **b**, Cross-sectional TEM image of a titanium–platinum SEA stack. The layer of titanium is 3 nm and the layer of platinum is 7 nm thick. **c**, SEAs operation in the oxygen-species absorption regime: at more negative electrical potentials, SEAs are flat while at more positive potentials, they curl. **d**, Curvature of a 70 μm × 16 μm SEA bending around the long axis versus voltage in the oxygen-species adsorption regime. Images of the cantilever bending are shown in the inset. Bending takes place over a narrow range of voltages, roughly 200 mV, and the curvature is well described by a logistic function (equation (1)). **e**, Actuation over many repeated cycles. The response is highly reproducible in the voltage windows used here, with devices cycling hundreds of times without degradation. **f**, The characteristic response time for switching between flat or curled in response to a step in actuation voltage (here a step between −0.2 V to −0.1 V) for a 55 μm × 10 μm bending around the short axis. Response times are between 10 and 100 ms (here 50 ms) and are set by the stiffness of the actuator and the viscosity of the liquid (Methods).

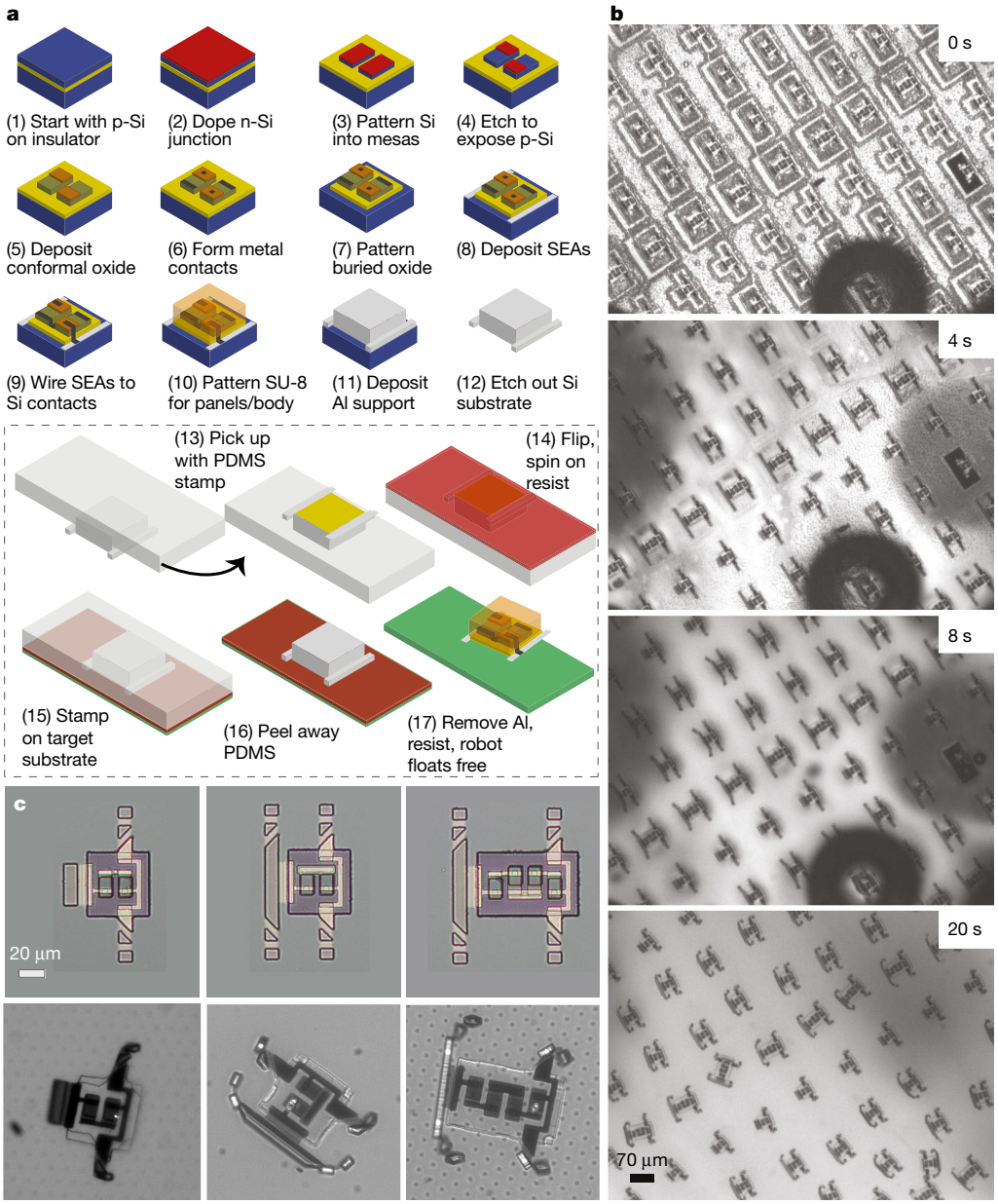

Fig. 3 | Microscopic robot fabrication and release. a, Schematic of the fabrication process (Methods). It features three main steps: fabricating the electronics, fabricating the legs and releasing the devices. The main fabrication steps are done at the wafer level and the release steps are typically done on diced chips. **b**, Optical images of the release process (Supplementary Video 3). In 20 s, robots go from bound to the surface to freely floating, folded and ready to walk. The yield is roughly 90%. **c**, Optical images of three robot designs before and after release.

and robustness. To our knowledge, no other actuator combines these properties. Piezoelectric actuators, while excellent for millimetre-scale robots, have not been scaled thin enough to operate at micrometre radii of curvature[22–24]. Thermal actuators—though useful in microelectromechanical systems and millimetre-scale robots[25]—are inefficient and difficult to address uniquely at small sizes due to the rapid diffusion of heat. Microactuators built using conducting polymers have similar characteristics in terms of voltage, power and curvature because they too exploit electrochemically induced stresses[26,27]. However, conducting polymer materials are harder to integrate in a silicon processing environment because they are damaged by standard chemicals for microfabrication, in particular solvents, developer and etchants[28]. Finally, actuators based on optical[29,30], acoustic[31,32], magnetic[33,34], thermal[34,35] or chemical[34,36–38] fields have enabled microswimmers[33], grippers[34,36] and other machines at the cellular scale[1,37], but cannot be controlled via onboard electronics.

To demonstrate the potential of SEAs, we fabricate a prototype microscopic robot that walks when illuminated by a sequence of laser pulses, as introduced in Fig. 1. We begin with a p-type silicon-on-insulator wafer, and then use standard doping, lithography and metallization (Fig. 3a, steps (1)–(7)) to create the robot's onboard circuitry, in this case, the silicon photovoltaics (characterized in Extended Data Fig. 6) and associated wiring (Methods). Once the silicon processing is complete, we deposit and pattern the legs, first building the SEAs (Fig. 3a, step (8)) followed by the rigid panels (Fig. 3a, step (10)). We emphasize that the processes for the legs are 'back-end': we only fabricate actuators and panels after all of the electronic elements are built. By keeping process temperatures low (<250 °C), these steps do not harm the previously fabricated electronics and are fully compatible with accommodating more complex complementary metal–oxide–semiconductors (CMOSs) in the future. In other words, a broad range of CMOS electronics could be patterned instead of simple photovoltaics and SEAs could be attached using the exact same process flow.

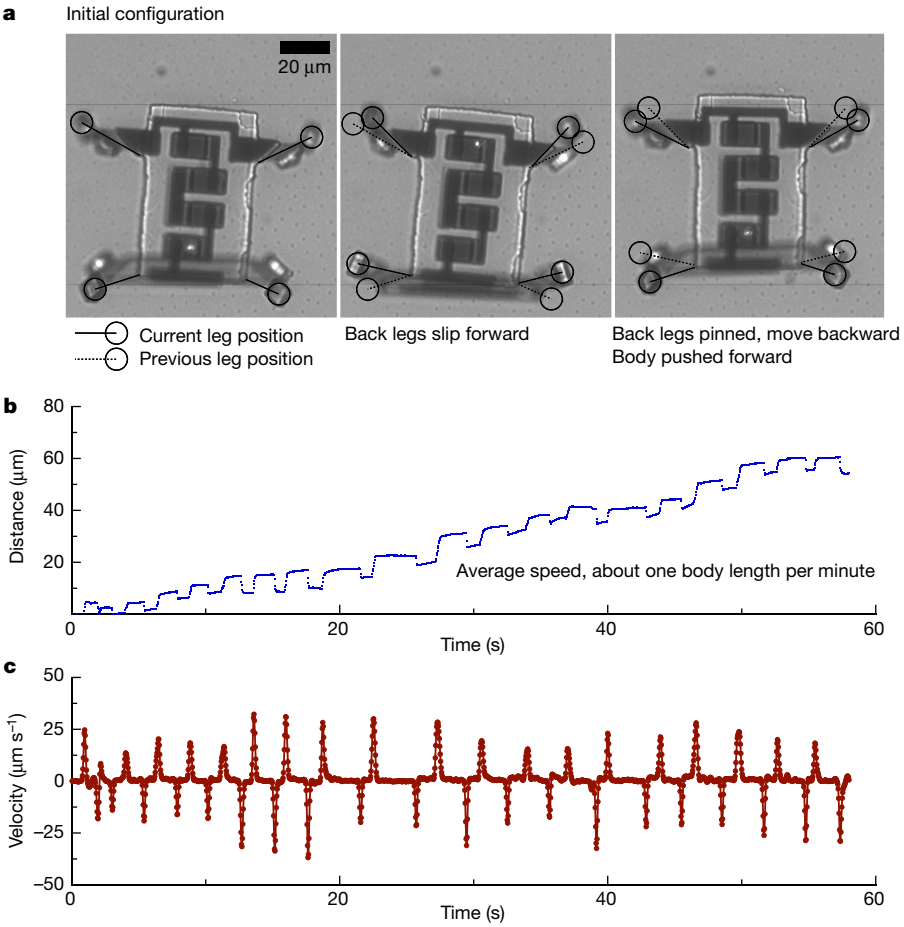

Fig. 4 | Microscopic robot locomotion. a, Optical images of a walking microscopic robot. This montage shows the position of the legs in the current position (solid lines) and previous position (dashed lines). Here a laser beam is steered by galvanometer-controlled mirrors, allowing a user to manually activate specific photovoltaics on a robot's body. When we direct light to the front photovoltaic, the back legs slip as they move forward. When we direct light to the back, the robot takes its power stroke: the back legs push off the substrate and propel the robot forward. The motion of the front legs changes the normal loading at the feet, causing the back legs to slip on the forward stroke and stick on the power stroke. **b**, Distance moved by the centre of mass of the walking microscopic robot as a function of time (measured from a fixed origin). On average, the robot travels at 1 μm s^{-1}, a speed comparable to crawling biological microorganisms. This speed is currently set by the laser switching time. **c**, Instantaneous velocity obtained by differentiating the data in **b**. Instantaneous speeds can be as large as 30 μm s^{-1}.

The last fabrication step is freeing the robots from the substrate without damage. We use a novel three-stage process to achieve this objective (Fig. 3a, steps (11)–(17))[39]. First, we sputter and pattern a 200-nm-thick layer of aluminium on top of the robots as a mechanical support. Then we remove the underlying silicon by xenon difluoride vapour phase etching. Once the robots have been undercut, we pick them up with a polydimethylsiloxane (PDMS) stamp[39], spin-coat a photoresist adhesive layer on top of the robots and stamp the resist–robot–aluminium layer onto a target substrate. The resist sticks to the substrate, attaching the robots when the PDMS is peeled away. Finally, we wet etch the aluminium and photoresist successively to release the robots into solution. Selected images from this process are shown in Fig. 3b and a video of the release process followed by robots self-folding is shown in Supplementary Video 3. Typical yields are 90%.

Fully formed microscopic robots are shown in Fig. 3c. The robot bodies have a maximum thickness of 5 μm (Fig. 1b), and width and length dimensions of 40 μm and 40 μm or 40 μm and 70 μm, respectively, depending on the number of photovoltaics onboard. They use their legs to walk on textured surfaces, as shown in Fig. 4 and Supplementary Videos 4–6. We focus laser light onto photovoltaics that bias either the front or back legs in sequence. In this configuration, each leg acts as the counterelectrode to the other: if one leg is positively biased, the other is negatively biased. We show the motion of the legs and a qualitative description of how they produce locomotion in Fig. 4a. The position and the velocity of the robot as a function of time are shown in Fig. 4b, c, respectively, with peak speeds approaching 30 μm s^{-1} and an average speed of about 1 μm s^{-1}, roughly one body length per minute. Extended Data Fig. 7 gives peak speed distributions for different surfaces and robot types. In general, the maximum speed is limited by a force balance between frictional contacts at the feet and viscous drag from the moving body (Supplementary Information).

The actuators, fabrication protocols and parallel release strategy presented here provide a complete processing scheme for semiconductor-based robots that are ten times smaller than the period at the end of this sentence. These sub-100 μm robots use onboard electronics to control actuation. Furthermore, these microscopic robots are remarkably robust. As they are made from highly stable materials, we find that they readily survive 200-K temperature variations and 13 orders of magnitude in acid concentration (see Methods for discussion). In addition, microscopic robots can safely be drawn into pipettes or syringes and injected out like chemicals (Supplementary Video 7). They are small enough to fit through the narrowest (34 gauge) hypodermic needles and maintain mechanical functionality after injection (Supplementary Video 8).

The simple microscopic robots demonstrated here are of limited function: at present, they are much slower than most swimming

microrobots[3], they lack the control of magnetically steered microrobots[33,40] and they do not sense their enviroment[2,3,29]. However, as they are compatible with standard CMOS processing, their capabilities can rapidly evolve. Future designs can immediately leverage 50 years of research in semiconductor electronics, manufacturing, packaging and integration technologies, and complimentary optical[29,30], acoustic[31,32], magnetic[33,34], thermal[34,35] or chemical[34,36,37] strategies for microrobotics. For example, microscopic robots equipped with thousands of onboard transistors, powered only by ambient sunlight, are readily achievable using existing CMOS circuits: all of the power for actuation and computation can be accommodated with roughly 10 nW while sunlight incident on a 30-μm photovoltaic supplies nearly 100 nW (see Methods for a discussion). Such robots could autonomously explore a microenvironment or directly interact with biological systems using local sensory input and feedback. Furthermore, we estimate that such microscopic robots can be manufactured at a cost that is much less than a penny per robot (≪US$0.01) using commercial silicon foundries (Supplementary Information). The new actuators and fabrication protocols presented here provide key elements needed to realize this remarkable future, taking a substantial step towards silicon-based, functional robotic systems that are too small to be resolved by the naked eye.

Online content

Any methods, additional references, Nature Research reporting summaries, source data, extended data, supplementary information, acknowledgements, peer review information; details of author contributions and competing interests; and statements of data and code availability are available at https://doi.org/10.1038/s41586-020-2626-9.

1. Ceylan, H., Giltinan, J., Kozielski, K. & Sitti, M. Mobile microrobots for bioengineering applications. *Lab Chip* **17**, 1705–1724 (2017).
2. Li, J., de Ávila, B. E.-F., Gao, W., Zhang, L. & Wang, J. Micro/nanorobots for biomedicine: delivery, surgery, sensing, and detoxification. *Sci. Robot.* **2**, eaam6431 (2017).
3. Palagi, S. & Fischer, P. Bioinspired microrobots. *Nat. Rev. Mater.* **3**, 113–124 (2018).
4. Hu, C., Pané, S. & Nelson, B. J. Soft micro-and nanorobotics. *Annu. Rev. Control Robot. Auton. Syst.* **1**, 53–75 (2018).
5. Wang, W., Duan, W., Ahmed, S., Mallouk, T. E. & Sen, A. Small power: autonomous nano-and micromotors propelled by self-generated gradients. *Nano Today* **8**, 531–554 (2013).
6. Theis, T. N. & Wong, H.-S. P. The end of Moore's law: a new beginning for information technology. *Comput. Sci. Eng.* **19**, 41–50 (2017).
7. Yeric, G. Moore's law at 50: Are we planning for retirement? In *2015 IEEE Intl Electron Devices Meeting (IEDM)* 1.1.1–1.1.8 (IEEE, 2015).
8. Wu, X. et al. A 0.04 mm^3 16 nW wireless and batteryless sensor system with integrated Cortex-M0+ processor and optical communication for cellular temperature measurement. In *2018 IEEE Symp. VLSI Circuits* 191–192 (IEEE, 2018).
9. Funke, D. A. et al. A 200 μm by 100 μm smart dust system with an average current consumption of 1.3 nA. In *2016 IEEE Intl Conf. Electronics, Circuits and Systems (ICECS)* 512–515 (IEEE, 2016).
10. Lee, S. et al. A 250 μm × 57 μm microscale opto-electronically transduced electrodes (MOTEs) for neural recording. *IEEE Trans. Biomed. Circuits Syst.* **12**, 1256–1266 (2018).
11. Seo, D., Carmena, J. M., Rabaey, J. M., Maharbiz, M. M. & Alon, E. Model validation of untethered, ultrasonic neural dust motes for cortical recording. *J. Neurosci. Methods* **244**, 114–122 (2015).
12. Viswanath, R. N., Kramer, D. & Weissmüller, J. Adsorbate effects on the surface stress–charge response of platinum electrodes. *Electrochim. Acta* **53**, 2757–2767 (2008).
13. Viswanath, R. N., Kramer, D. & Weissmüller, J. Variation of the surface stress–charge coefficient of platinum with electrolyte concentration. *Langmuir* **21**, 4604–4609 (2005).
14. Weissmüller, J. et al. Charge-induced reversible strain in a metal. *Science* **300**, 312–315 (2003).
15. Jin, H.-J. & Weissmüller, J. Bulk nanoporous metal for actuation. *Adv. Eng. Mater.* **12**, 714–723 (2010).
16. Sader, J. E. Surface stress induced deflections of cantilever plates with applications to the atomic force microscope: rectangular plates. *J. Appl. Phys.* **89**, 2911–2921 (2001).
17. Tamayo, J., Ruz, J. J., Pini, V., Kosaka, P. & Calleja, M. Quantification of the surface stress in microcantilever biosensors: revisiting Stoney's equation. *Nanotechnology* **23**, 475702 (2012).
18. Conway, B. E., Birss, V. & Wojtowicz, J. The role and utilization of pseudocapacitance for energy storage by supercapacitors. *J. Power Sources* **66**, 1–14 (1997).
19. Wiggins, C. H. & Goldstein, R. E. Flexive and propulsive dynamics of elastica at low Reynolds number. *Phys. Rev. Lett.* **80**, 3879–3882 (1998).
20. Felgner, H., Frank, R. & Schliwa, M. Flexural rigidity of microtubules measured with the use of optical tweezers. *J. Cell Sci.* **109**, 509–516 (1996).
21. Ananthakrishnan, R. & Ehrlicher, A. The forces behind cell movement. *Int. J. Biol. Sci.* **3**, 303–317 (2007).
22. Piazza, G., Felmetsger, V., Muralt, P., Olsson, R. H. III & Ruby, R. Piezoelectric aluminum nitride thin films for microelectromechanical systems. *MRS Bull.* **37**, 1051–1061 (2012).
23. Sinha, N. et al. Piezoelectric aluminum nitride nanoelectromechanical actuators. *Appl. Phys. Lett.* **95**, 053106 (2009).
24. Zaghloul, U. & Piazza, G. 10–25 nm piezoelectric nano-actuators and NEMS switches for millivolt computational logic. In *2013 IEEE 26th Intl Conf. Micro Electro Mechanical Systems (MEMS)* 233–236 (IEEE, 2013).
25. Ebefors, T., Mattsson, J. U., Kälvesten, E. & Stemme, G. A walking silicon micro-robot. In *Proc. 10th Intl Conf. Solid-State Sensors and Actuators (Transducers '99)* 1202–1205 (1999).
26. Jager, E. W., Inganäs, O. & Lundström, I. Microrobots for micrometer-size objects in aqueous media: potential tools for single-cell manipulation. *Science* **288**, 2335–2338 (2000).
27. Jager, E. W., Smela, E. & Inganäs, O. Microfabricating conjugated polymer actuators. *Science* **290**, 1540–1545 (2000).
28. Smela, E. Microfabrication of PPy microactuators and other conjugated polymer devices. *J. Micromech. Microeng.* **9**, 1–18 (1999).
29. Palagi, S. et al. Structured light enables biomimetic swimming and versatile locomotion of photoresponsive soft microrobots. *Nat. Mater.* **15**, 647–653 (2016).
30. Dai, B. et al. Programmable artificial phototactic microswimmer. *Nat. Nanotechnol.* **11**, 1087–1092 (2016).
31. Ahmed, D. et al. Selectively manipulable acoustic-powered microswimmers. *Sci. Rep.* **5**, 9744 (2015).
32. Rao, K. J. et al. A force to be reckoned with: a review of synthetic microswimmers powered by ultrasound. *Small* **11**, 2836–2846 (2015).
33. Tottori, S. et al. Magnetic helical micromachines: fabrication, controlled swimming, and cargo transport. *Adv. Mater.* **24**, 811–816 (2012).
34. Leong, T. G. et al. Tetherless thermobiochemically actuated microgrippers. *Proc. Natl Acad. Sci. USA* **106**, 703–708 (2009).
35. Baraban, L. et al. Fuel-free locomotion of Janus motors: magnetically induced thermophoresis. *ACS Nano* **7**, 1360–1367 (2013).
36. Bassik, N. et al. Enzymatically triggered actuation of miniaturized tools. *J. Am. Chem. Soc.* **132**, 16314–16317 (2010).
37. Miskin, M. Z. et al. Graphene-based bimorphs for micron-sized, autonomous origami machines. *Proc. Natl Acad. Sci. USA* **115**, 466–470 (2018).
38. Solovev, A. A., Sanchez, S., Pumera, M., Mei, Y. F. & Schmidt, O. G. Magnetic control of tubular catalytic microbots for the transport, assembly, and delivery of micro-objects. *Adv. Funct. Mater.* **20**, 2430–2435 (2010).
39. Carlson, A., Bowen, A. M., Huang, Y., Nuzzo, R. G. & Rogers, J. A. Transfer printing techniques for materials assembly and micro/nanodevice fabrication. *Adv. Mater.* **24**, 5284–5318 (2012).
40. Wu, Z. et al. A swarm of slippery micropropellers penetrates the vitreous body of the eye. *Sci. Adv.* **4**, eaat4388 (2018).

Methods

Microrobot fabrication protocol

We start with commercially produced silicon-on-insulator wafers (Ultrasil Corporation). The device layer is p-type (boron doped) and has a thickness of 2 μm and a resistivity 0.1 ohm-cm. The buried oxide layer is 500 nm thick and the handle layer is 500 μm thick. We form p–n junctions by depositing 550 nm of phosphosilicate glass (5% by weight phosphorus glass) at 350 °C with plasma-enhanced chemical vapour deposition using phosphine/helium plasma. We diffuse dopants into the device layer by annealing the substrate at 1,000 °C for 3 min in argon with a rapid thermal annealer, using a ramp rate of 75 °C s^{-1}. After doping, we remove the phosphosilicate glass using 6:1 buffered oxide etch.

The major steps are as follows: selectively remove portions of the n-layer to provide contact points with the underlying p-silicon; selectively remove the unwanted p-type silicon, defining the photovoltaic's structure; electrically isolate the p–n junction with a conformal dielectric layer; make electrical contacts to the p-type and n-type silicon; pattern the buried oxide layer; deposit the platinum layer for the SEAs; pattern the platinum layer; pattern/deposit the capping layer of the SEAs; interconnect the SEAs to the silicon photovoltaics; dice the 4-inch wafer into 12 mm test die; pattern the SU-8 encapsulation layer and rigid panels; mechanically support the devices with patterned aluminium before release; release devices from the fabrication substrate; stamp devices onto target substrates; release the devices into solution.

A full fabrication protocol is available at Protocol Exchange[41].

SEA structure and thickness characterization

We use X-ray reflectometry thickness and resistivity measurements to characterize the ALD platinum layer growth as a function of the number of ALD cycles. (Extended Data Fig. 1). We find the growth can be separated into two phases: a nucleation phase and a bulk growth phase. Resistivity measurements (via four-point probe) confirm that there is a critical number of cycles (around 30) for a continuous electrical film to form.

To image the cross-section of the titanium–platinum bimorph using transmission electron microscopy (TEM; Fig. 2b, Extended Fig. 2a), we deposit 20 cycles of Al_2O_3 followed by 70 cycles of platinum on a bare silicon wafer. Then we sputter 3 nm of titanium on top of the platinum to form a SEA. We next put an amorphous carbon layer (Sharpie marker) on top of the titanium to protect the samples. We mill a thin cross-sectional lamina from the top of the sample using an ion beam (Thermo Fisher Helios G4 UX FIB) and attach it to a copper TEM grid by using a nanomanipulator. Finally, we use an ion beam to thin the lamina to electron transparency. To create the electron energy loss spectra image and spectra for the cross-section of the sample (Extended Fig. 2a), we collect data with a Gatan Quefina dual electron energy loss spectrometer using 0.25 eV per channel.

For in-plane TEM imaging (Extended Data Fig. 2b), we deposit 70 cycles of platinum on an 80-nm-thick silicon nitride membrane supported by silicon (from Greater Grids). We then image the layers in scanning TEM mode on a probe-corrected TEM (Thermo Fisher Titan Themis Cryo S/TEM) at 120 kV.

Experimental setup for electrochemical characterization

To test the SEAs, we use a computer-controlled d.c. voltage source (Yokagawa 7651). One lead of the voltage source is wired to a high-impedance platinum-iridium microprobe (Microprobes for Life Science). The probe is coated with paralyne so that only a small area (about 1 μm^2) of the tip is exposed, guaranteeing the majority of current measured comes from the test device (about 100-μm^2 area). The second lead from the voltage source is wired to a silver/silver chloride (Ag/AgCl) pellet, about 1 mm in size (purchased from Warner Scientific). The large size ratio between the actuator and the pellet makes the actuator the highest-impedance element in the circuit. Thus, applied voltages are almost entirely borne by the actuator. To measure current simultaneously with voltage, we introduce, in series with the voltage source, a preamplifier (Ithaco 1211) sharing a common ground and record the preamp output with an oscilloscope (picoScope 5200). The low currents flowing through the system (nanoampere) eliminate the need for a three-electrode system (as is typical for ultramicroelectrodes).

Regimes of actuation for SEAs

SEAs bend in response to three different electrochemical effects: adsorption of hydrogen, adsorption of oxygen species and electrochemical oxidation, as shown in Fig. 2, Extended Data Fig. 4. Each of these mechanisms occurs at a different applied voltage relative to the solution, and each is well documented in the electrochemical literature[12–15]. At large positive voltages, the platinum oxidizes, and both the cyclic voltammogram and the SEA curvature are highly hysteretic (Extended Data Fig. 4a). We do not consider the oxidization regime in this work and it will be explored in a subsequent publication.

Extended Data Fig. 4b shows a cyclic voltammogram and corresponding curvature for a titanium–platinum SEA over a voltage range covering the two quasi-reversible regimes of adsorption. Hydrogen and oxygen-species adsorption/desorption occur in the range −0.8 V to −0.5 V and −0.2 V to 0.2 V versus Ag/AgCl, respectively, consistent with results for bulk platinum[12].

The oxygen-species adsorption/desorption regime is explored in more detail in Extended Data Fig. 5. The cyclic voltammogram for a SEA across this voltage range at a sweep rate of 400 mV s^{-1} is shown in Extended Data Fig. 5a. The current is dominated by the Faradic electrochemical processes at the platinum–electrolyte interface (see 'Model for bending due to electrochemical adsorption' for further discussion). Extended Data Fig. 5b shows the SEA curvature and the non-Faradic capacitive contribution to the current. The latter was obtained by fitting an interpolating polynomial to the forward and backward sweep individually, and then averaging the two curves and finally subtracting this contribution. Note this approach assumes transients that occur when the voltage sweep changes direction decay rapidly.

The capacitive current probes both the double-layer capacitance and any charge transfer processes associated with surface adsorption. We find a peak in capacitive current in the same voltage region where the SEAs bend. We associate this peak with charge transfer from the oxygen species upon adsorption. The dashed lines are a fit to a standard adsorption model[18,42]:

$$I_c = \frac{e^2 \alpha \Omega}{k_B T n} \frac{\exp\left(\frac{-e}{k_B T n}(V - V_0)\right)}{\left(1 + \exp\left(\frac{-e}{k_B T n}(V - V_0)\right)\right)^2},$$

where Ω is the density of bonding sites for adsorbates and α is the voltage sweep rate. Fitting the peak near bending yields a surface charge due to the adsorption in the oxygen regime of $e\Omega \approx 130$ μC $cm^{-2} \approx 8$ charges per nm^2. This is consistent with previous measurements of oxygen-species adsorption. For example, literature values for H_2O/OH^- adsorption[43,44] range from 110 μC cm^{-2} to 160 μC cm^{-2}, whereas phosphate ions adsorb[45] to a maximum density of 137 μC cm^{-2}.

SEA stability in chemical and thermal environments

Our experiments covered a range of different chemical compositions and found no noticeable change in the actuator response. In particular, we tested SEAs in phosphoric acid mixtures (pH 1 to 5), strong sodium hydroxide (pH 13 to 14), phosphate-buffered saline (pH 7.6) and dilute hydrochloric acid (HCl; pH 1 to 5). In each case, we found that the SEA could be reproducibly actuated, without damage, for the duration of an experiment (typically thousands of cycles). We also soaked devices overnight in strong HCl (pH 0), transferred them to higher-pH solutions and found no noticeable degradation. In addition, our devices

are deposited at 275 °C, which makes thermal degradation unlikely given that the device must operate in water. We do find that damage and hysteresis can occur if the device is biased to extremely large potentials. In this regime, the platinum begins to oxidize, and the actuator becomes hysteretic. In other words, the actuator does not return to its rest position when the voltage is turned off. This residual curvature can accumulate over cycles, preventing the device from opening and closing. For extreme potentials (about 1 V), the device can fail after 10–100 cycles.

Force and stiffness characterization of SEAs

To characterize the stiffness of the actuators, we measure the exponentially decaying transient response to a sudden step in voltage. The characteristic timescale is set by the elasticity of the actuator and the viscous drag from the liquid:

$$\tau_{act} = \frac{11}{60}\frac{\pi\mu L^4}{Dw\log\left(\frac{4L}{\pi w}\right)},$$

where L is the length of the actuator, w is the width of the actuator and μ is the viscosity of water. Details of this method are provided in refs. [19,20].

Figure 2e shows the transient response for a 7-nm-thick, 55-μm-long and 8-μm-wide platinum–graphene actuator; the fit gives a decay time $\tau = 50$ ms. From the equation above, this yields a bending energy $D = 5.4 \times 10^{-15}$ J. Similar measurements on different geometry cantilevers yield comparable results. From these measurements and neglecting the bending stiffness of the graphene capping layer, we infer the Young's modulus for the ALD platinum of $E_y = 0.18$ TPa. This is in reasonable agreement with the accepted bulk value of platinum, 0.17 TPa.

Given this value for D, we can use equation (1) and the measured curvature (Fig. 2d) to infer the surface stress γ_m associated with oxygen-species adsorption. We find $\gamma_m = 0.3$ N m^{-1}. This value is consistent in scale with previous work on adsorption-induced stresses in bulk platinum actuators: typical literature values range from 0.1 to 3.0 N m^{-1} (refs. [13,14,46,47]). Finally, we can determine the force generated by SEAs. Specifically, a force of:

$$F_b = Dw\frac{R_c^{-1}}{L} = \frac{\gamma_m t}{2}\frac{w}{L}$$

is required to push the cantilever back to its equilibrium position. We find a force of 1 nN for a roughly equal aspect ratio cantilever of 7 nm thickness. This puts SEAs at a scale comparable to cell–cell adhesive forces[21] and about ten times larger than typical maximum optical trap forces.

The characteristic timescale for motion and maximum force allow us to estimate the order of magnitude for the actuator efficiency. As the actuator is essentially a cantilever, it stores an energy of $\frac{1}{2}DwR_c^{-2}L$ when bending. Moving at its peak speed generates a mechanical power on the order of $\frac{1}{2}DwR_c^{-2}L/\tau_{act}$. Compared with the electrical power required to operate the actuator, we find an efficiency of

$$\frac{1}{2}\frac{DR_c^{-2}}{P_d\tau_{act}} \approx \frac{\gamma_m^2}{P_d\mu}\frac{t^2 w\log\left(\frac{4L}{\pi w}\right)}{L^4},$$

where P_d is the fixed power density due to electrochemistry (see 'Regimes of actuation for SEAs'). Numerically, we find this efficiency is on the order of 10^{-3} to 10^{-4}. More accurate measures of efficiency require specifying the task the actuator is performing, its actual rate of motion and the driving power supply. In addition, the electrical power required to drive the actuator has a capacitive contribution from the charge stored via surface adsorption, which can be become comparable to the power from background electrochemistry at high driving frequencies (>30 Hz). In practice, we point out that given the low power budget, efficiency is not typically a concern: a nanowatt of power is easily accommodated even if most of the energy is not converted to work.

Model for bending due to electrochemical adsorption

We assume that electrochemically active species in the solution are able to adsorb to the surface of the platinum via a charge transfer reaction. In the oxygen-species regime, adsorption typically follows a reaction of the form

$$MA + e^{-1} \rightleftharpoons M + A^-,$$

where A represents the adsorbate (for example, OH^-, HSO_4^- or $H_2PO_4^-$) and M denotes an adsorption site. The fraction of sites occupied by an adsorbate, φ, for an ideal adsorption process is given by[18,42]

$$\varphi = \frac{1}{1+\exp\left(\frac{-e}{k_BT}(V-V_0)\right)},$$

where V is the applied voltage and V_0 is an offset voltage set by the free energy of adsorption, electrode composition and solution chemistry.

To connect to experimental data for curvature, we assume that the change in the surface-stress difference between the two sides of the stack is proportional to the number of occupied sites: $\Delta\gamma = \gamma_m\varphi$. The sign convention is such that the platinum expands when oxygen-species adsorb. To link the $\Delta\gamma$ to the curvature (R_c^{-1}) we use Stoney's equation[17]

$$\Delta R_c^{-1} = \frac{\Delta\gamma t}{2D}.$$

After simplifying, we find:

$$\Delta R_c^{-1} = \frac{\gamma_m t}{2D}\frac{1}{1+\exp\left(\frac{-e}{k_BT}(V-V_0)\right)}.$$

A similar derivation applies for other adsorption reactions that occur at more negative voltage ranges (less than −0.5 versus Ag/AgCl), like hydrogen.

In practice, we find that the curvature changes over a wider range of voltages than predicted by the ideal adsorption process described above. We account for this deviation by introducing a phenomenological non-ideality factor, n, such that

$$\Delta R_c^{-1} = \frac{\gamma_m t}{2D}\frac{1}{1+\exp\left(\frac{-e}{k_BTn}(V-V_0)\right)}.$$

For the processing conditions used here, we that find n is typically between 1.2 and 1.7. For example, the graphene–platinum actuators in Fig. 2 are best fit with $n = 1.2$ while the titanium–platinum actuators in Supplementary Fig. 4 are better fit with $n = 1.7$. In general, we find that different processing conditions can lead to larger values for n: depending on how the platinum is processed, n can be upwards of 3 to 4, suggesting the onset of multiple electron reactions. Processing can impact the platinum surface by changing the surface chemistry and/or creating surface inhomogeneities that broaden the width of the transition.

Analysis of maximum robot walking speed

The maximum speed for the robot's centre of mass is constrained by friction and drag. The robot body moving over the substrate below shears the water in between, creating a drag force

$$F_d = \frac{v\mu A}{d},$$

where v is the velocity, A is the area of the body and d is the gap between the robot's body and the substrate. The frictional contacts at the robot's

feet can balance this force, unless it exceeds the slip condition $F_f < \eta F_n$ where η is the friction coefficient and F_n is the normal force on the robot body. Taking the force of gravity as the dominant normal load gives a maximum speed for the robot:

$$v < \frac{\eta mgd}{\mu A},$$

where g is the gravitational acceleration constant. Experimentally, we find top speeds depend on the patterned surface roughness: when walking across arrays of random dots, as in Supplementary Fig. 8, the robot's speed is never greater than about 40 μm s^{-1}, whereas for hexagonal arrays, the top speed is about 25 μm s^{-1}. Given the weight of 50 pN and an estimated gap height $d \approx 10$ μm, these speeds correspond to effective friction coefficients of $\eta \approx 0.25$ and $\eta \approx 0.16$, respectively. For bare glass, the frictional interaction is too low to support walking at a measurable speed: we find the robot slips rather than walks.

The forces required to walk at these speeds are much lower than the peak forces generated by SEAs. As noted earlier, SEAs are capable of producing forces approaching 1 nN, roughly 20 times larger than the weight of the robot body. If limited by the actuator performance, instead of friction, future microrobots could walk nearly 20 times faster. Balancing drag resistance against peak actuator force, instead of friction, predicts a peak speed of about 1 mm s^{-1}, nearly 10 body lengths per second. Future designs could potentially reach this limit by increasing the frictional loads, either by adding weight to the robot or by coupling the normal load to the lateral motion with lubrication forces.

Complexity and cost of future generations of microscopic robots

Assuming a 180-nm CMOS fabrication process performed at a foundry, we estimate that an autonomous microscopic robot, roughly 100 μm on a side, with a clock, sensors and a programable controller would cost approximately US$0.001 and be capable of operating with sunlight as its sole power source.

To estimate the cost, we take a baseline number of US$10 per cm^2 for 180-nm CMOS lithography performed at a foundry at production scale. Given that each robot is on the order of 100 μm on a side, we expect 10,000 robots per cm^2, yielding US$0.001 per robot.

Broadly, a 180-nm CMOS process allows transistors on the order of 1 μm on a side. Thus, a 100-μm robot can accommodate circuits with tens of thousands of transistors, offering a high degree of flexibility. Specific examples of the necessary electronics for an autonomous robot, clocks, sensors and controllers can be found in the literature. Clocks that generate voltage pulses suitable for walking (about 200 mV at 10–100 Hz), about 20 μm on a side, have been built using a variety of architectures[48–50] and typical designs consume 1–10 nW of power. Such clocks can be integrated with sensors and controllers to form microsystems and computers, as established in the smart-dust and micromotes literature. For example, Funke et al.[9] demonstrated a fully integrated clock, chemical sensor and finite state machine, built in 180-nm CMOS, that fits within a 100 × 200 $μm^2$ area and operates at about 3 nW. In a larger space, about 360 × 400 $μm^2$, Wu et al.[8] demonstrated a fully integrated microcontroller, temperature sensor, 4 kB of static random-access memory, a clock and two-way communication via micro-light-emitting diodes, made with 55-nm CMOS, and operating at power budget of 16 nW.

As all of these example circuits operate at less than 100 nW, a robot using these onboard systems could be powered by sunlight. Daylight provides roughly 1 kW m^{-2} of incident power. Given a photovoltaic on the order of 30 μm on a side with a 10% conversion efficiency, the robot would collect roughly 100 nW, nearly an order of magnitude more power than needed for the combined energy cost of sensing, computation and actuation.

Data availability

The authors declare that the data supporting the findings of this study are available within the paper and its supplementary information files. Source data are provided with this paper.

41. Miskin, M. Z. et al. Fabrication of electronically integrated, mass-manufactured, microscopic robots. *Protoc. Exch*. https://doi.org/10.21203/rs.3.pex-1012/v1 (2020).
42. Conway, B. E. Electrochemical oxide film formation at noble metals as a surface-chemical process. *Prog. Surf. Sci*. **49**, 331–452 (1995).
43. Climent, V., Gómez, R., Orts, J. M. & Feliu, J. M. Thermodynamic analysis of the temperature dependence of OH adsorption on Pt (111) and Pt (100) electrodes in acidic media in the absence of specific anion adsorption. *J. Phys. Chem. B* **110**, 11344–11351 (2006).
44. van der Niet, M. J., Garcia-Araez, N., Hernández, J., Feliu, J. M. & Koper, M. T. Water dissociation on well-defined platinum surfaces: the electrochemical perspective. *Catal. Today* **202**, 105–113 (2013).
45. Gisbert, R., García, G. & Koper, M. T. Adsorption of phosphate species on poly-oriented Pt and Pt (111) electrodes over a wide range of pH. *Electrochim. Acta* **55**, 7961–7968 (2010).
46. Lafouresse, M., Bertocci, U. & Stafford, G. Dynamic stress analysis applied to (111)-textured Pt in $HClO_4$ electrolyte. *J. Electrochem. Soc*. **160**, H636–H643 (2013).
47. Raiteri, R. & Butt, H.-J. Measuring electrochemically induced surface stress with an atomic force microscope. *J. Phys. Chem*. **99**, 15728–15732 (1995).
48. Funke, D. A. et al. Ultra low-power, -area and -frequency CMOS thyristor based oscillator for autonomous microsystems. *Analog Integr. Circuits Signal Process*. **89**, 347–356 (2016).
49. Hwang, C., Bibyk, S., Ismail, M. & Lohiser, B. A very low frequency, micropower, low voltage CMOS oscillator for noncardiac pacemakers. *IEEE Trans. Circ. Syst. I Fundam. Theory Appl*. **42**, 962–966 (1995).
50. Galea, F., Casha, O., Grech, I., Gatt, E. & Micallef, J. Ultra low frequency low power CMOS oscillators for MPPT and switch mode power supplies. In *14th Conf. Ph.D. Research in Microelectronics and Electronics (PRIME)* 121–124 (IEEE, 2018).

Acknowledgements We acknowledge the CNF staff, in particular T. Pennell, J. Clark, V. Genova, C. Alpha and G. Bordonaro, for guidance and support with the fabrication process; S. Norris and B. Bircan for discussions; funding from the Army Research Office (ARO W911NF-18-1-0032), the Air Force Office of Scientific Research (AFSOR) MURI Grant FA2386-13-1-4118, the Cornell Center for Materials Research DMR-1719875, NSF Grant DMR-1435829 and the Kavli Institute at Cornell for Nanoscale Science. This work was performed at the Cornell NanoScale Facility, an NNCI member supported by NSF Grant NNCI-1542081.

Author contributions M.Z.M., P.L.M. and I.C. conceived the experiments. M.Z.M. designed and fabricated the robots, carried out the experiments, and collected and analysed the data. M.Z.M. and A.J.C. developed the silicon fabrication procedure. M.Z.M and K.D. developed the platinum actuator fabrication procedure. M.Z.M, M.F.R. and Q.L. interpreted the platinum electrochemistry data. E.P.E., Q.L. and M.C. took TEM images characterizing the ALD platinum. M.Z.M., I.C. and P.L.M wrote the manuscript with all authors contributing.

Competing interests The authors declare no competing interests.

Additional information

Supplementary information is available for this paper at https://doi.org/10.1038/s41586-020-2626-9.

Correspondence and requests for materials should be addressed to M.Z.M., P.L.M. or I.C.

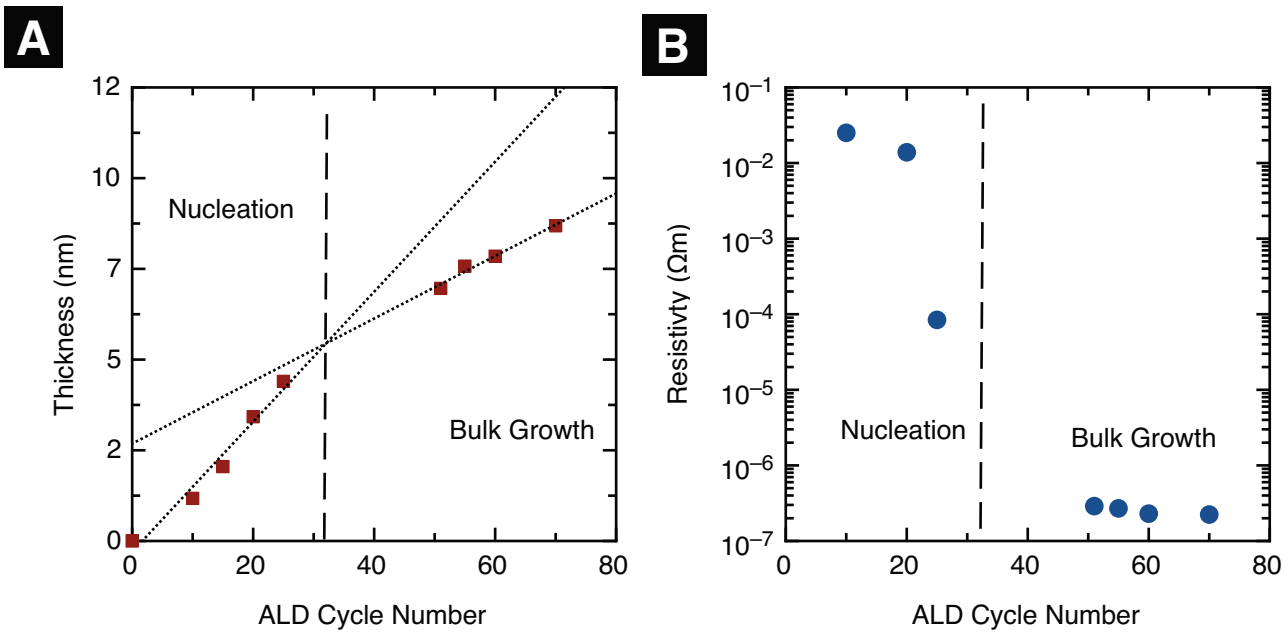

Extended Data Fig. 1 | Characterization of the ALD platinum layers. a, X-ray reflectometry thickness measurements as a function of the number of growth cycles of ALD. The first 30 cycles are a nucleation phase where the film grows rapidly in thickness. Once the surface is covered in platinum, a bulk growth phase begins at a slower rate. **b**, Resistivity measurements (via four-point probe) as a function of ALD cycle number. We interpret the dramatic drop in resistivity after about 30 cycles as clear evidence that a continuous electrical film has formed.

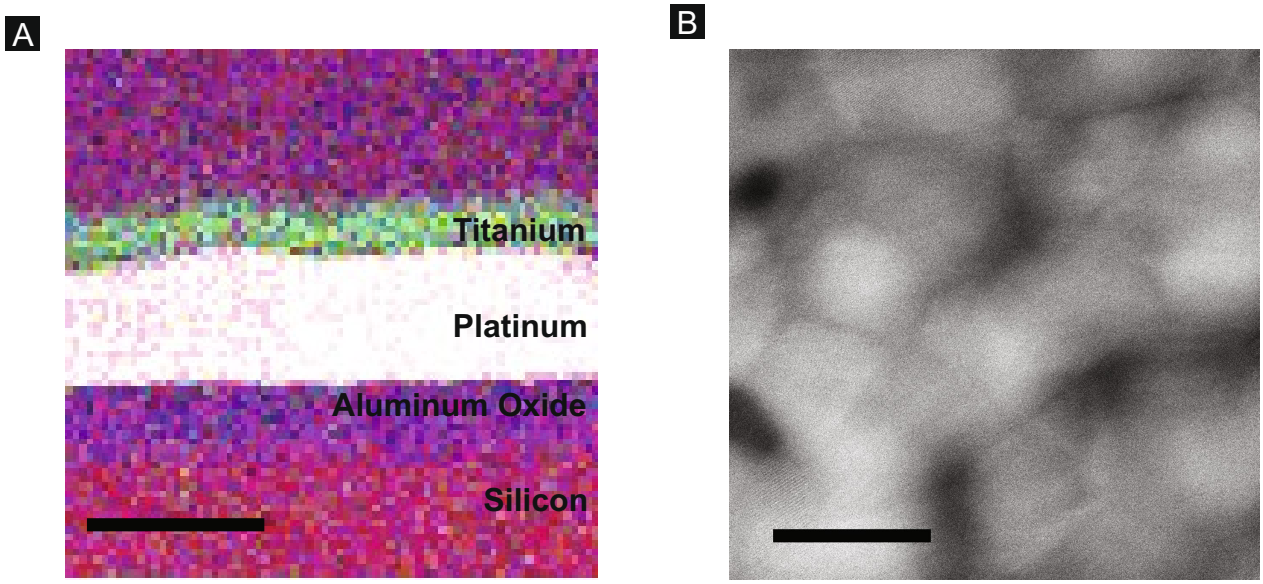

Extended Data Fig. 2 | TEM imaging of SEA structure and morphology. **a**, Cross-sectional TEM image of a titanium–platinum SEA structure, with colours coded by electron energy loss spectroscopy. Silicon is shown in red, titanium in green, oxygen in blue and platinum in white. **b**, In-plane TEM image of an ALD platinum film showing crystal grain sizes of approximately 10 nm. Scale bars, 10 nm.

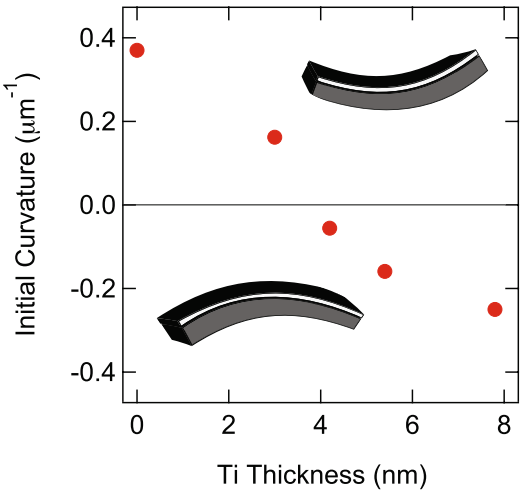

Extended Data Fig. 3 | Controlling SEA pre-stress. The curvature in a SEA is set by both adsorption of ions and pre-stresses built up during fabrication. Here we plot the curvature of a titanium–platinum SEA in the absence of any applied bias as a function of the titanium layer thickness. The curvature varies continuously from positive to negative as the titanium layer is increased. As the voltage is fixed to the open circuit potential, this effect is purely due to pre-stress. The sign of the curvature inverts at a titanium thickness of around 4 nm. Overall, the pre-stress provides an added level of control over the three-dimensional structure formed using SEAs and rigid panels.

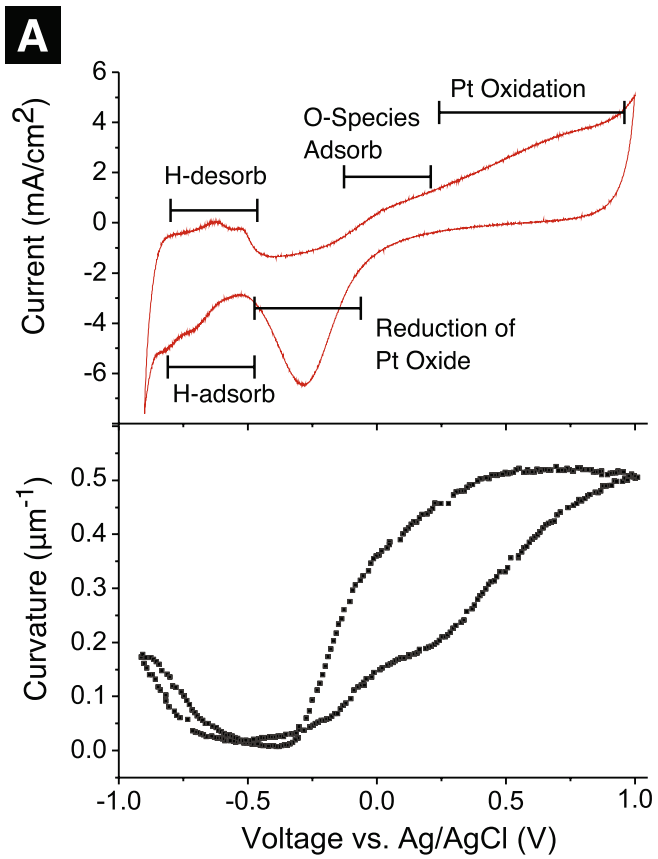

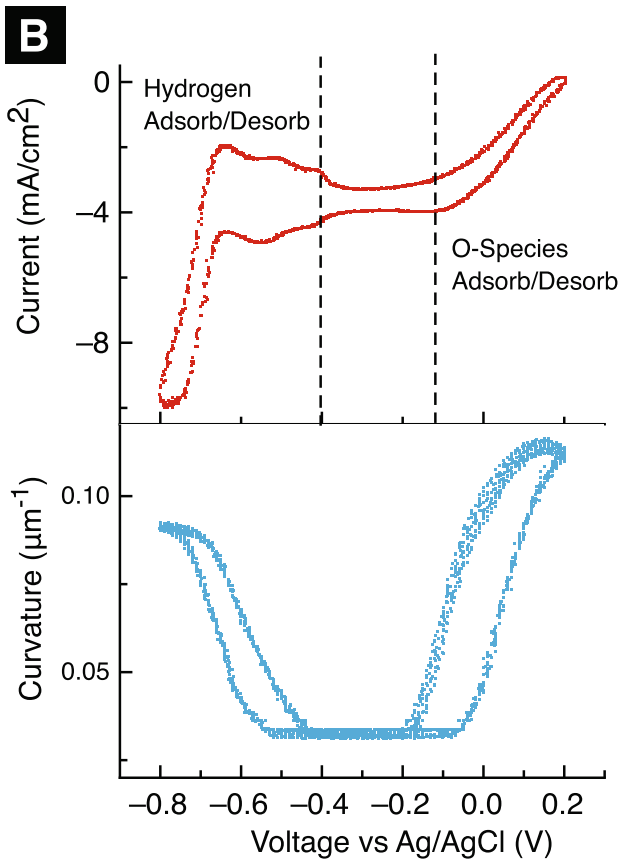

Extended Data Fig. 4 | Irreversible and quasi-reversible actuation of SEAs. **a**, Top: cyclic voltammogram of a titanium–platinum SEA over a large voltage range versus Ag/AgCl, swept at 1 V s^{-1}. Standard features of platinum electrochemistry are observed: hydrogen adsorption and desorption peaks from about −0.5 V to −0.9 V and a broad peak at positive voltages that includes both oxygen-species adsorption and later oxidation of the platinum. When the sweep returns from the oxidation regime, there is an oxide reduction peak at about −0.3 V. Bottom: the curvature of a SEA over the same range, showing strong hysteresis in the platinum oxidation regime. **b**, Top: cyclic voltammogram for a titanium–platinum SEA, sweep rate 400 mV s^{-1}, over a narrower sweep range, avoiding oxidation of the platinum. We find that the cyclic voltammogram is relatively reversible in both the hydrogen and oxygen adsorption/desorption regimes. Bottom: the curvature of a SEA over the same quasi-reversible range of voltages. We observe two branches of actuation, the hydrogen and oxygen-species adsorption regimes, each with a small amount of hysteresis. All measurements were performed in phosphate-buffered saline solution.

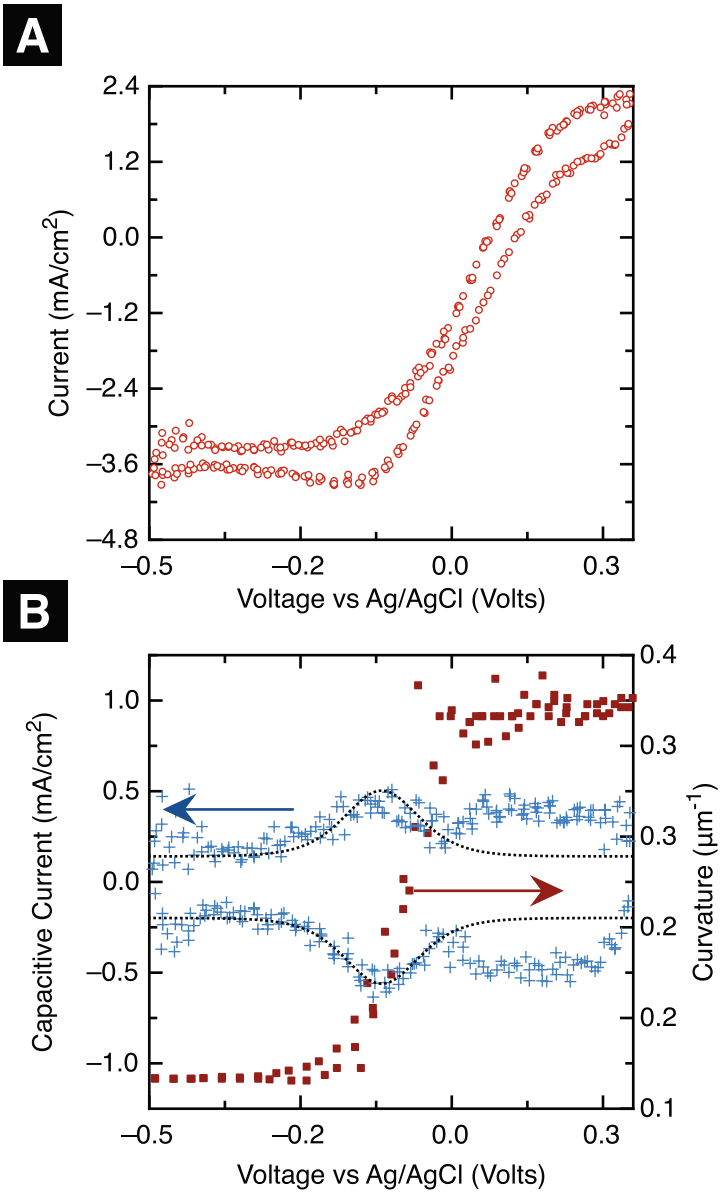

Extended Data Fig. 5 | Electrochemistry in the oxygen species adsorption region. a, Cyclic voltammogram for a graphene–platinum SEA that is 70 μm long and 13 μm wide over the voltage range used here to actuate the robots: the oxygen-species adsorption/desorption regime. **b**, The SEA curvature (red dots) and the capacitive portion of the response (blue crosses). The latter is obtained by removing current that does not depend on the voltage sweep direction (Methods). A peak in charge transfer occurs in the same region where bending takes place. The integrated magnitude of charge transferred gives a surface charge density of 130 μC cm^{-2}, consistent with typical values for oxygen-species adsorption[43–45] The data are well represented by a standard charge transfer model with nearly ideal adsorption (dashed lines) (Methods).

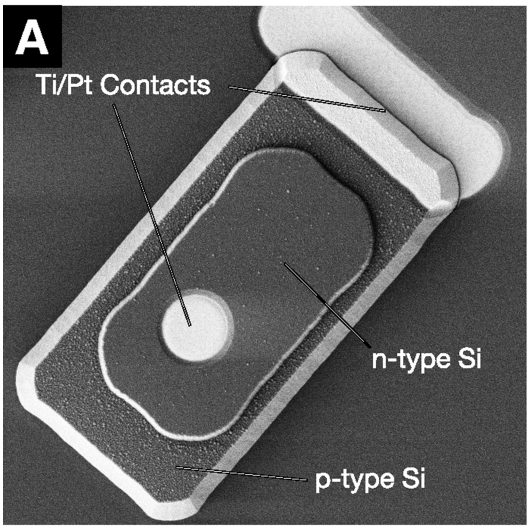

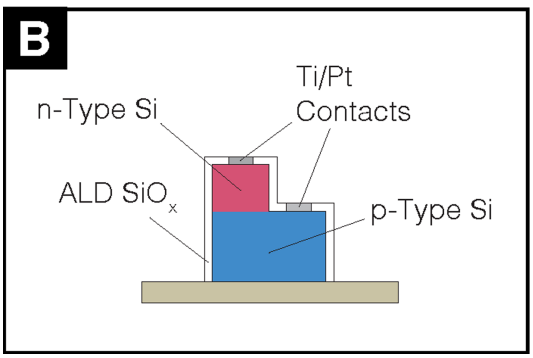

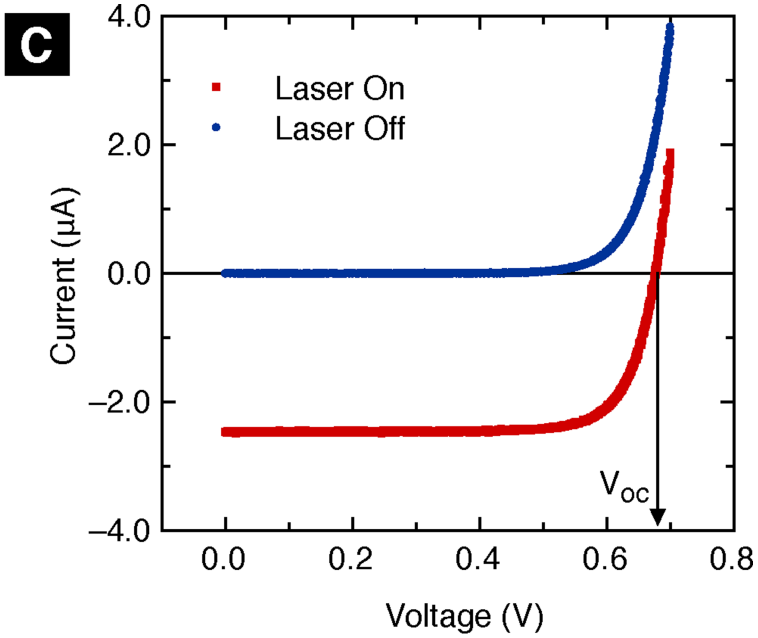

Extended Data Fig. 6 | Photovoltaic characterization. a, A labelled scanning electron microscopy image of a silicon photovoltaic, 10 μm by 20 μm in size. **b**, A schematic cross-section of one of our photovoltaics. **c**, A current–voltage curve for a photovoltaic with (red curve) and without (blue curve) illumination. The devices were illuminated by a 785-nm wavelength laser with an intensity of 100 nW μm^{-2}. The illuminated current–voltage curve shows an open circuit voltage (V_{oc}) of approximately 700 mV.

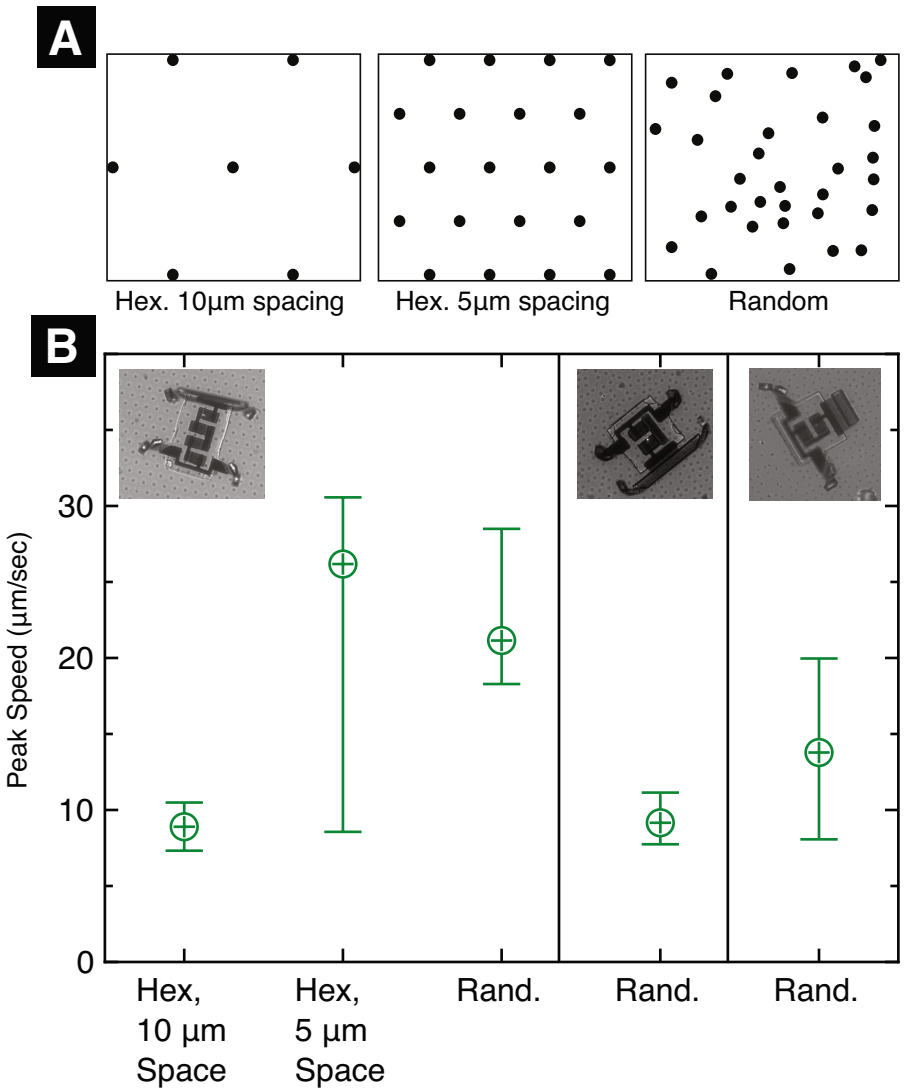

Extended Data Fig. 7 | Peak walking speeds on different textured surfaces. **a**, Schematics of the three surfaces robots walked on: hexagonal arrays of knobs spaced 5 µm apart and 10 µm apart, and random arrays of knobs. **b**, We measure the maximum lateral velocity a robot takes at each step, then aggregate the results into a distribution of peak speeds for each robot body type and frictional surface type (robot types are depicted in the inset images). The upper and lower error bars represent the upper and lower quartiles. Substantial variability is expected for walking on rough surfaces: each step can provide a different contact geometry and force. The order of magnitude is constrained by an interplay between friction and drag: the robot speed is bounded by the maximum frictional force the feet can generate. The maximum frictional force is found to be 0.1–0.3 of the robot's weight, consistent with friction. (See Methods for a detailed discussion).